Two-photon Photo-emission of Ultrathin Film PTCDA Morphologies on Ag(111)

Aram Yang, Steven T. Shipman[†], Sean Garrett-Roe[‡]
James Johns, Matt Strader, Paul Szymanski[§],
Eric Muller, and Charles Harris[*]

Department of Chemistry, University of California, Berkeley, California 94720 and

Chemical Sciences Division, Lawrence Berkeley National Laboratory, Berkeley, California, 94720

November 29, 2007

,

Abstract

Morphology- and layer-dependent electronic structure and dynamics at the PTCDA/Ag(111) interface have been studied with angle-resolved two-photon photoemission. In Stranski-Krastanov growth modes, the exposed wetting layer inhibited the evolution of the vacuum level and valence band to bulk values. For layer-by-layer growth, we observed the transition of electron structure from monolayer to bulk values within eight monolayers. Effective masses and lifetimes of the conduction band and the $n = 1$ image potential state were measured to be larger for disordered layers. The effective mass was interpreted in the context of charge mobility measurements.

Keywords: Organic-thin film, electronic-structure, dispersion, lifetimes, interface, charge-mobility

[†]Current address: Department of Chemistry, University of Virginia, Charlottesville, VA 22904.

[‡]Current address: University of Zurich, Physikalisch-Chemisches Institute, Winterthurerstrasse 190, 8057 Zurich, Switzerland.

[§]Current address: Department of Chemistry, Brookhaven National Laboratory, Upton, NY 11973.

[*]Corresponding author: cbharris@berkeley.edu

1 Introduction

The potential assembly of electronic and optoelectronic devices from organic semiconductors has driven considerable research into the behavior of electrons in molecular thin films. While bulk electronic properties of molecular crystals are generally well-understood, in the reduced dimensionality of molecular devices electronic behavior is inherently different and merits its own investigation [1]. In ultrathin films, charge transport properties are affected by the structure of the adsorbate and the strength of adsorption, which often depend on the underlying substrate and its crystal face[3, 4]. The substrate may support interfacial states (occupied or not) including the image potential state (IPS), and interact with the adsorbate to create substrate- and crystal face- specific electronic levels. The substrate also affects interfacial charge carrier properties through the energetic alignment of its Fermi level to the adsorbate. However, the chemical properties of the adsorbate molecule and interface do not solely account for the electronic properties at an interface.

Within the last few years, the study of molecular crystals has focused on the relationship between morphology and electronic properties. A positive correlation between crystallinity and electron mobility has created interest in monitoring deposition rates and substrate temperatures, which affect the quality of the deposited layer[5]. Crystal defects, grain boundaries, and molecular orientation can inhibit charge mobility by several orders of magnitude. Grain size has been demonstrated to affect mobility[6, 7]. Energetic disorder affects charge injection into an organic semiconductor[8], and islanding on top of a substrate can lead to electron confinement[9, 10]. The intermolecular crystal packing affects the degree of orbital overlap and, consequently, charge transport properties in organic semiconductors[11]. Identifying molecules suitable for use in devices thus relies on understanding the effects of morphology, geometry, and layer thickness on molecular electronic properties.

In order to create cheap, easily manufactured, and stable organic solid state devices,

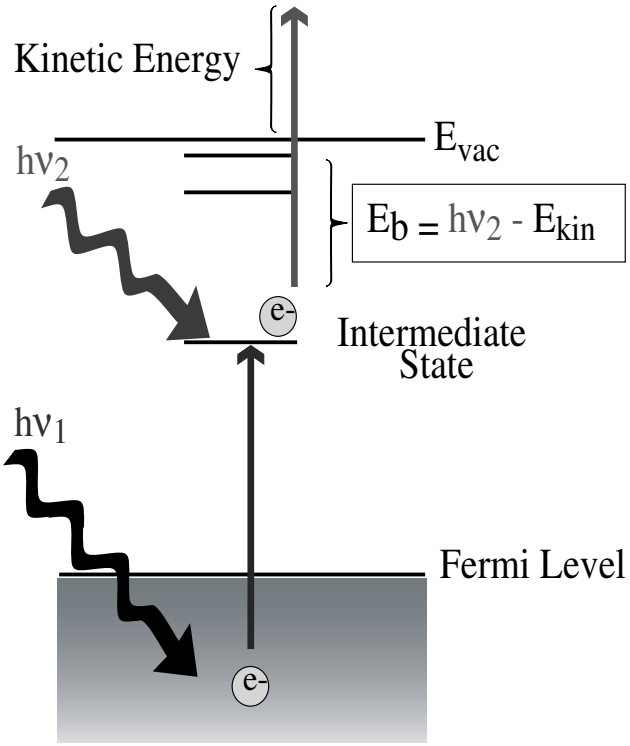

Figure 1: A pump laser pulse, $h\nu_1$, excites an electron from below the Fermi level into an intermediate state. A second probe laser pulse, $h\nu_2$, photo-emits the electron.

research attention has focused on several classes of molecules. Of particular interest are molecular thin films composed of semi-conducting planar aromatic hydrocarbons, which show promise for use in field-effect transistors, light emitting diodes, and photovoltaic cells[12]. A prototype for this class of hydrocarbons is 3,4,9,10-perylene-tetracarboxylic dianhydride (PTCDA) (fig. 2). This molecule is cheap to produce, absorbs in the visible spectrum, and resists photo-degradation. Its herringbone structure and quasi-epitaxial growth on various substrates have been characterized at length and allow for controlled layer deposition[13, 14, 15]. The electronic structure of PTCDA has been studied in the bulk phase and at several interfaces[16, 17, 18, 19], and measurements of charge transport properties are reported in the literature[20]. Several recent studies have examined interfacial states of PTCDA specific to the Ag(111) surface that are hybrid states of PTCDA bulk electronic states mixing with the Ag 5sp band[21, 22].

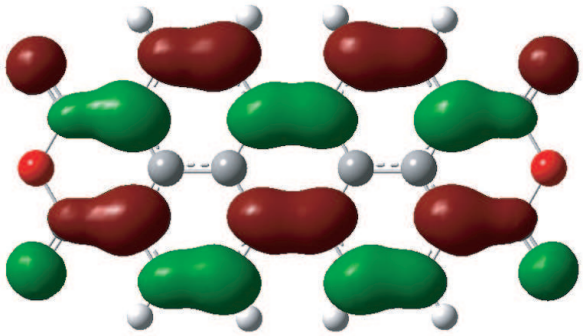

(a)

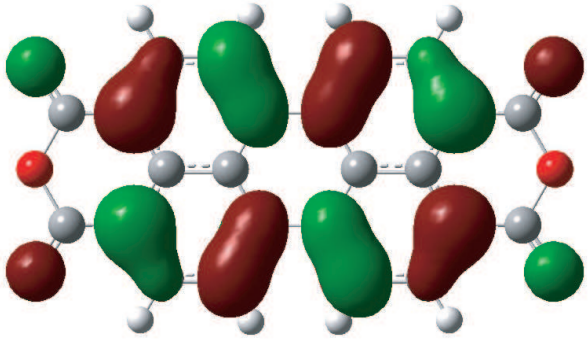

(b)

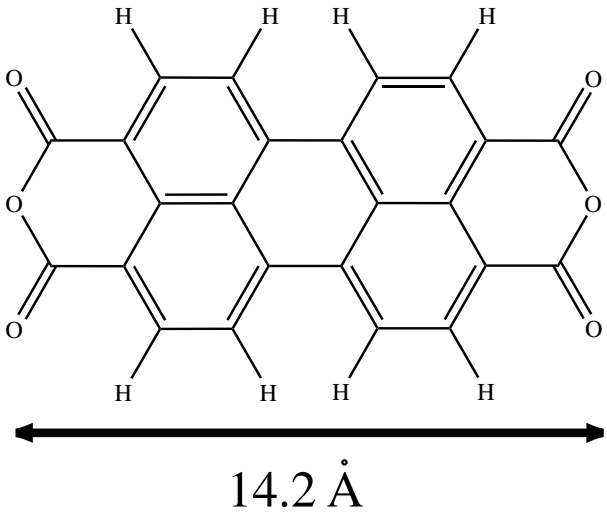

(c)

Figure 2: (a) The PTCDA LUMO. (b) The PTCDA HOMO. (c) PTCDA skeleton.

PTCDA layers exhibit different growth modes on Ag(111), depending on the substrate temperature during dosing (T_D). Krause et al.[15] have published AFM studies of temperature-dependent morphologies of PTCDA on Ag(111), with average thicknesses of 50 Å. The morphological regimes include a mesa-like structure at $T_D = 135$ K with small islands arranged along the silver substrate steps; a smooth surface at room temperature; and a faceted surface at 333 K leading to a transition at 343 K to islands growing on top of a complete 'wetting layer,' i.e., Stranski-Krastanov growth. The wetting layer in this morphology is two monolayers thick. Islands range in size from 0.1 μm^2 at 343 K to 5 μm^2 at 413 K, and island densities range from 12 μm^{-2} at 343 K to 0.001 μm^{-2} at 413 K. The crystallinity of the layer also increases with higher substrate temperatures. Ferguson and Jones have studied the effects of growth temperature and morphology on optical properties of bulk films (>100 nm thickness), with the results that increased low-energy absorption, enhanced blue-shifted emission, and longer fluorescence decays correspond to increases in the dosing temperature[23]. In this paper, we have probed different morphologies of ultrathin films of PTCDA at the Ag(111) surface with angle-resolved two-photon photo-emission (2PPE) to study the effects of morphology on lifetimes and effective masses of unoccupied states.

Two-photon photo-emission is a pump-probe spectroscopy capable of probing both unoccupied and initially occupied states[2] at an interface, including metal surface states and molecular orbital-based states of an adsorbate, while simultaneously obtaining dynamical information. A fundamental step to understanding the processes of charge transport at a metal-organic interface is the characterization of charge injection from a cathode into a molecular layer, which can be modelled with 2PPE. The addition of angular resolution enables electronic band mapping of ultrathin films. In a 2PPE experiment, an intermediate excited state is populated with a pump laser pulse ($h\nu_1$) which has less energy than the workfunction (Φ), after which a second, probe pulse ($h\nu_2$) photo-emits the electron from the intermediate state (fig. 1). The kinetic energy of a photo-electron is recorded, and a binding energy (E_b) relative to the vacuum energy is determined by subtracting a photon energy

from the kinetic energy. When $h\nu_1$ and $h\nu_2$ are both capable of photo-emitting an intermediate state electron, the appropriate photon energy to subtract is determined by changing the photon energies of both pulses by different amounts and mapping the resultant shifts in peak kinetic energies. For example, if $h\nu_1$ is changed by $\Delta h\nu$, and $h\nu_2$ by $2\Delta h\nu$, then an intermediate state photo-emitted by $h\nu_1$ will shift in kinetic energy by $\Delta h\nu$, and a state photo-emitted by $h\nu_2$ will shift in kinetic energy by $2\Delta h\nu$. To resolve band masses, photo-electron kinetic energies (E_{kin}) are measured at different angles (θ) between the substrate surface normal and the detector. From the angular dependence of the kinetic energies, the effective mass (m^*) of the photo-electron can be determined according to the relation:

$$E_{\mathrm{kin}} = E_{\mathrm{b}} + \frac{(\hbar k_{\parallel})^2}{2m^*}, \tag{1}$$

where $k_{\parallel}$ is the electron wave vector parallel to the surface and calculated with:

$$k_{\parallel} = \sqrt{\frac{2m_{\mathrm{e}}E_{\mathrm{kin}}}{\hbar^2}}\sin\theta. \tag{2}$$

An electron delocalized along the surface will have an effective mass approximately equal to the free electron mass (m_e) and its energy will vary parabolically with $k_{\parallel}$. A spatially localized electron is characterized by large values of m^* and therefore its energy remains constant over a range of $k_{\parallel}$.

2 Experimental

Detailed descriptions of the lasers and of the molecular beam epitaxy (MBE) and ultra-high vacuum (UHV) systems have been published elsewhere[33]. In short, a pulse from a commercial ultrafast oscillator is amplified, and parametric amplification is used to generate tunable ultrafast pulses of $\sim$100 fs duration from 480 – 720 nm. This pulse is then doubled in a BBO crystal, after which it is spatially separated from the frequency-doubled pulse via dichroic mirrors, and temporally separated using a Klinger translation stage. The two beams are re-overlapped to photo-emit electrons. The kinetic energy of these electrons is determined

by measuring electron time-of-flight from the sample to our homebuilt detector. In this paper, the results are dependent only on the material system and not on the wavelength of light used, and so the fundamental visible pulse will be labeled $h\nu_1$ and the frequency-doubled pulse will be referred to as $h\nu_2$.

PTCDA was obtained from both TCI America and Fluka and was outgassed at 380 K for 24 hours in a Knudsen cell maintained at ultrahigh vacuum (10^{-9} torr). Each source yielded identical results. The effusion cell was connected to the main chamber with a gate valve capable of isolating the main chamber from the effusion cell. Additionally, a shutter placed before the Knudsen cell provided a more sensitive mechanism for stopping deposition, and the gate valve and shutter were used simultaneously to control dosing. The source material was maintained at 638 K during dosing, while the substrate temperature was varied from 130 K – 540 K in order to control growth morphology. The morphologies are referred to by the substrate temperature while dosing, e.g., $T_D = 140$ K indicates the layer-by-layer growth exhibited at a substrate dosing temperature of 140 K. Experiments were concentrated on four substrate temperatures: $T_D = 140$ K, $T_D = 200$ K, $T_D = 300$ K, and $T_D = 450$ K. LEED and Auger were used to monitor surface structure and composition, respectively. Adsorption and desorption temperatures for the first few monolayers were determined by the appearance or quenching of peaks in the 2PPE spectrum, which also provided dosing calibration. We refer to layer thicknesses in units of overall monolayers (ML) dosed, with the recognition that the "monolayer" unit – a complete layer of one molecule thickness – is a misleading label for the actual thickness at the surface in the case of three-dimensional morphologies.

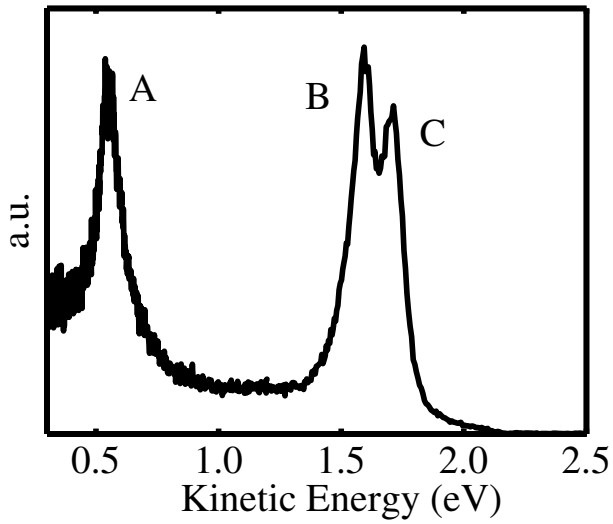

Figure 3: Peak A denotes a PTCDA molecular state. Peaks B and C are the $n = 1$ image potential state energies for 1 and 2 ML, which are both seen here as a result of incomplete layer-by-layer growth.

3 Results and Discussion

3.1 Workfunction and Vacuum Level Shifts

The kinetic energy spectrum for 1.5 ML, dosed at $T_D = 300$ K, is presented in figure 3. Peak A is identified as derived from a molecular state, peak B as the $n = 1$ IPS for 1 ML, and peak C is the $n = 1$ IPS for 2 ML. The appearance of peaks at separate energies is a distinguishing feature of layer-by-layer growth. Knowledge of the proper workfunction (Φ) of each layer is necessary to assign an accurate binding energy to each intermediate state. The shift in workfunction results from several factors. Hill et al.[34] report a surface dipole shift as a PTCDA layer is adsorbed on the surface, which creates a negative charge barrier at the surface. In addition, when PTCDA is dosed on a surface, the electronic levels of PTCDA may mix with the Ag 5sp band at the interface[21]. The shift in the vacuum level was determined for PTCDA by fitting the $n = 1$ and $n = 2$ image state binding energies to a hydrogenic progression:

$$E_{\mathrm{IPS}} = \frac{-0.85}{(n+a)^2} eV, \tag{3}$$

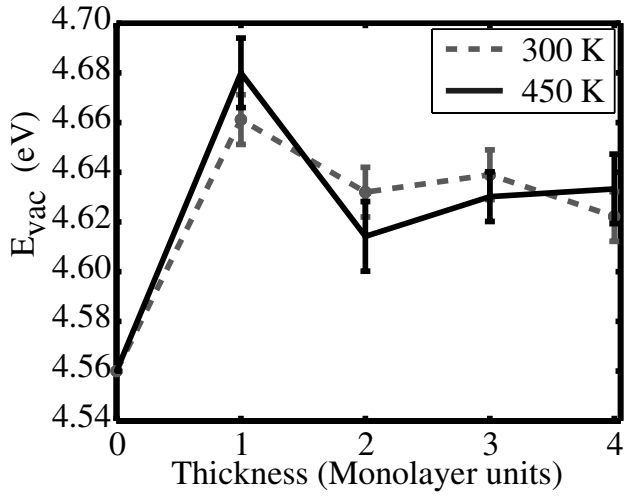

Figure 4: The layer-by-layer evolution of the vacuum level from Eqn. 3 for $T_D = 300$ K and $T_D = 450$ K, referenced to the clean silver value.

where a is a quantum defect parameter [35]. The shift in the vacuum level is the amount by which the experimental IPS energies must be shifted so that they fit a hydrogenic progression, since the convergence of higher-order IPS energies is pinned to the vacuum level.

The shifts in vacuum level (fig. 4) for $T_D = 300$ K and $T_D = 450$ K indicate that the first monolayer experiences negative charge transfer into the underlying Ag(111) surface, which creates a surface dipole that increases the vacuum level. Lower dosing temperatures resulted in spectra where the IPS were difficult to resolve and fit. By using equation 3, the vacuum level shift $\Delta\Phi$ for 1 ML is 0.11 eV with respect to the bare surface, and for 2 ML the total shift is 0.06 eV. The $n = 1$ IPS binding energy stays constant for thicker coverages, which suggests that the vacuum level has stopped shifting, but the $n = 2$ IPS is quenched by 3–4 ML in all coverages which precluded using Eq. 3. The shift in vacuum level is similar to vacuum level shifts for naphthalene [30] and benzene [28].

For cases where the necessary image potential states were not visible, the workfunction shift can be determined through the high-energy and low-energy cutoffs in 2PPE kinetic energy spectra. The width of the kinetic energy spectra subtracted from the energy of two UV photons is equivalent to the width of the unoccupied states. At the interface, this is

E_{VB} (eV)							
1 ML	2 ML	3 ML	4 ML	5 ML	6 ML	7 ML	8 ML
$T_D = 450$ K							
4.7±0.1	5.0±0.1	4.8±0.4	5.0±0.1	5.0±0.4	5.0±0.1	4.8±0.1	4.9±0.1
$T_D = 300$ K							
4.6±0.1	4.7±0.2	5.2±0.6	5.4±0.7	5.5±0.7	5.8±0.2	6.1±0.1	6.2±0.1
$T_D = 200$ K							
4.8±0.1	4.9±0.1	4.9±0.1	4.9±0.1	5.0±0.2	5.2±0.2	5.7±0.2	6.2±0.2
$T_D = 140$ K							
4.6±0.1	4.6±0.1	4.8±0.1	4.8±0.2	5.8±0.5	5.8±0.2	6.2±0.1	6.3±0.1

Table 1: The evolution of the unoccupied states E_{VB} as more PTCDA is dosed. The rise in E_{VB} occurs more rapidly for low T_D amorphous layers than for high T_D crystalline layers.

the distance from the Fermi level to the vacuum level, i.e., the workfunction. The changing unoccupied state width was used to track the evolution of the valence band as the PTCDA coverage was increased. An accelerating bias voltage can be applied to the sample such that both a low- and high-energy cutoff are present in 2PPE kinetic energy spectra. The width of the unoccupied states for each layer is initially close to the workfunction determined by IPS and is followed by a transition to the value for bulk PTCDA, except for the layer grown at $T_D = 450$ K (Table 1). As expected, thicker, layer-by-layer coverages converge to the bulk PTCDA workfunction value of 6.4 eV. The three-dimensional nature of high dosing temperature, Stranski-Krastanov growth can leave the wetting layer exposed, and the utility of measuring the scattering width of 2PPE kinetic energy spectra will be limited by the exposed wetting layer.

A wavelength survey was taken to help determine the proper binding energy of each peak. In figure 5(a), the 2PPE spectra at various wavelengths is presented, where the higher energy peak is the $n = 1$ IPS and lower energy peak is the LUMO+1, consistent with the results of Temirov et al.[22]; the peak assigment is discussed further below. By plotting the peak kinetic energies vs. the visible photon energies (fig. 5(b)), a slope of two is obtained for the LUMO+1, and a slope of unity for the IPS. The LUMO+1 is therefore photo-emitted by $h\nu_2$, and the IPS by $h\nu_1$. The binding energies of the $n = 1$ IPS are 0.82 eV (referenced to the

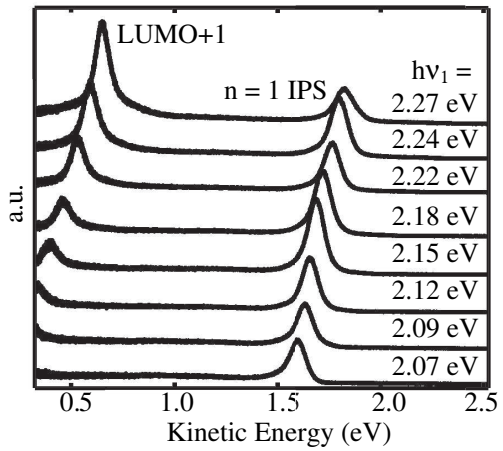

(a) Wavelength Survey

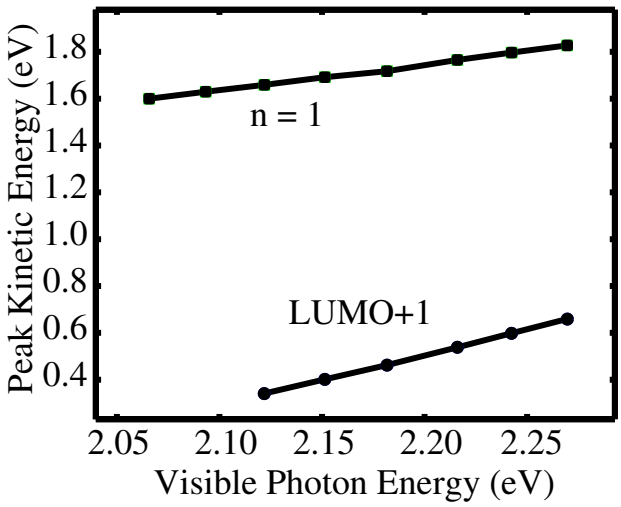

(b) Peak Energy vs. $h\nu_1$

Figure 5: (a) 2PPE spectra were obtained for a range of wavelengths, labeled by $h\nu_1$. (b) Using the slope of the peak kinetic energies vs. visible photon energies, we can determine if the state is probed by $h\nu_1$ or $h\nu_2$.

vacuum energy E_{vac}) at 1 ML and 0.68 eV for subsequent layers, across all morphologies. An IPS electron is sensitive to a dielectric layer between the electron and the metal substrate, and the uniformity of IPS binding energies indicates that the first two layers for all morphologies have negligible differences in dielectric constants due to morphology. However, the quenching of image potential states occurs at different layer thicknesses for each morphology.

For 1–2 ML dosed at temperatures less than 400 K, PTCDA lacks the energy to completely re-organize into a smooth wetting layer. Patches of 1 ML are left exposed in the wetting layer, and the $n = 1$ IPS at the 1 ML energy value is still visible after 2 ML has been dosed at $T_D < 400$ K. In a 2 ML thick layer in which both image states are visible, the 1 ML $n = 1$ state at 0.82 eV disappear if the layer is annealed above 450 K, and the population of $n = 1$ at 0.68 eV increases. LEED images corroborate that low T_D layers are initially amorphous, but align into a crystalline surface after annealing at higher temperatures. The $n = 1$ IPS is completely quenched by 20 ML at $T_D = 450$ K; 10 ML for $T_D = 300$ K; 4 ML for $T_D = 200$ K; and 3 ML for $T_D = 140$ K.

The electronic structure derived from molecular states varies more significantly with morphology. Peak A in figure 3, the LUMO+1 state, is present in crystalline layers, from which binding energies of 4.1 eV for 1 ML and 4.0 eV for 2 ML and thicker were obtained. Increasing the photon energy results in one-photon photo-emission, without the appearance of a new peak, but we label Peak A as the LUMO+1 in agreement with the energy levels in ref. [22] and consistent with Tautz et al.[21], who identify the lowest unoccupied state at the interface as a hybrid Ag-PTCDA state. For low T_D morphologies, a broadened electronic structure dominates the spectra at low kinetic energy, in lieu of a sharp peak (fig. 6). The broad structure disappears while a sharp peak grows in if the layer is annealed, with annealed spectra similar to spectra of a layer which had dosed at the annealing temperature. The origin of this manifold is unclear from 2PPE experiments; the simplest explanation is that it represents an inhomogeneously broadened peak resulting from scattering in an amorphous

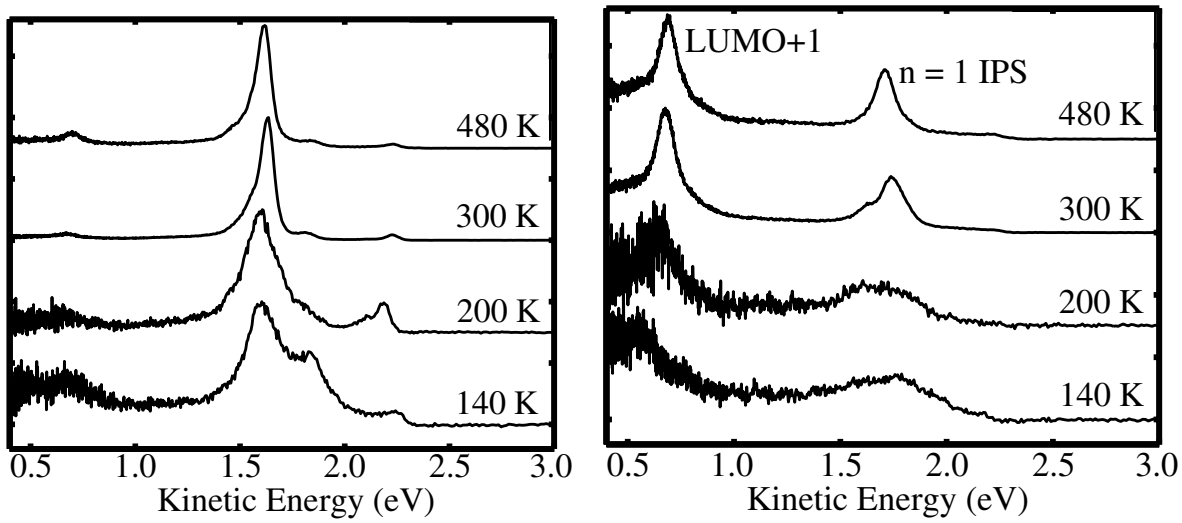

(a) One ML

(b) Two ML

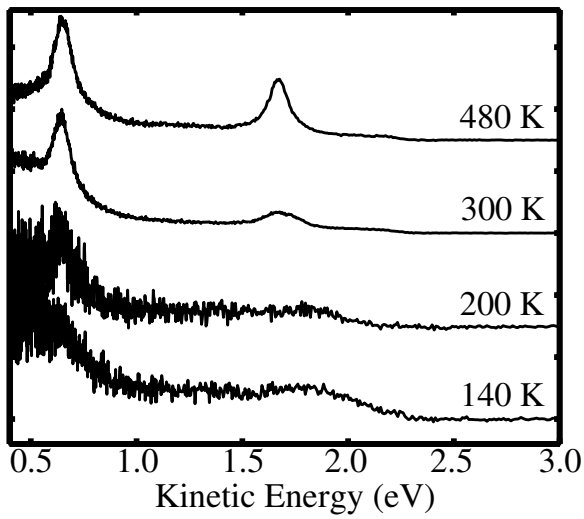

(c) Three ML

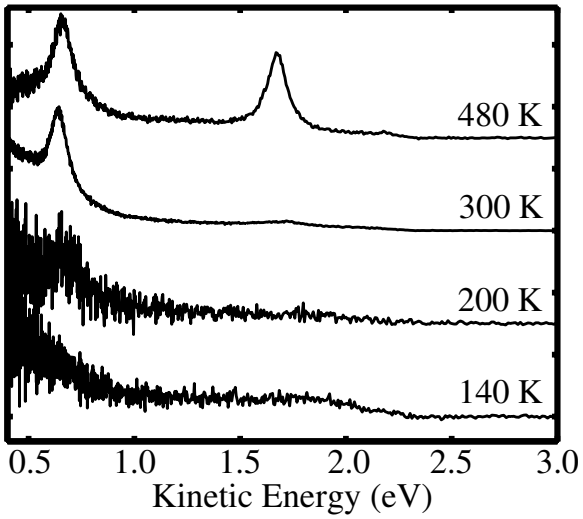

(d) Four ML

Figure 6: A stackplot comparison of 2PPE data for 1–4 ML of different PTCDA morphologies. The data have been normalized so that the maximum of each spectrum is unity. The $n = 1$ IPS is quickly extinguished in layer-by-layer growth at low T_D, and the LUMO+1 in crystalline layers is well-defined.

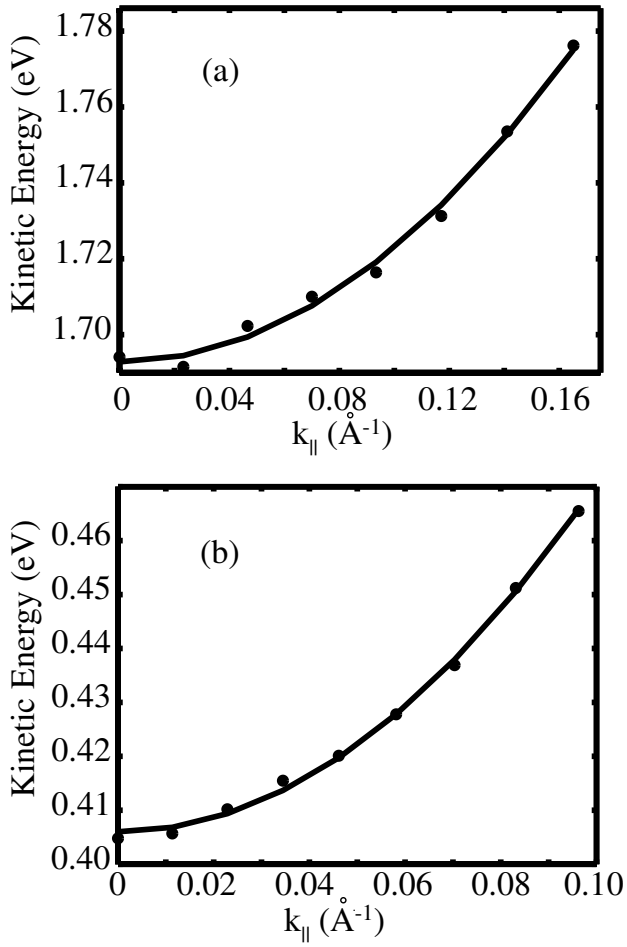

Figure 7: (a) The effective mass of the LUMO+1 at 2 ML is 0.58 m_e for T_D = 300 K. (b) The effective mass of $n = 1$ is 1.3 m_e for the same system.

layer. Interestingly, this manifold exhibits long time dynamics, as discussed below.

3.2 Effective Masses

The effective masses of each intermediate state were dependent on layer morphology. Generally, the intermediate states in crystalline layers were more dispersive than in amorphous layers. The 2PPE spectra were collected at 140 K – 150 K, to minimize the possibility of temperature-dependent band effects. The effective mass for the conduction band is lowest when the layer is most crystalline, which can be achieved with a high T_D or by annealing at elevated temperatures (> 400 K). The effective mass at 2 ML ranges from 0.74 m_e for T_D =

200 K to 0.52 m_e for $T_D = 450$ K. Molecular overlap should decrease with increasingly thick layers due to epitaxial strain; this is reflected in the increasing LUMO+1 effective mass with thicker layers. For the LUMO+1 state at $T_D = 300$ K, at 2 ML thickness the effective mass is 0.58 m_e (fig. 7a); 0.85 m_e at 4 ML; and 0.96 m_e at 6 ML thickness. At lower temperatures, the effective mass is difficult to fit given the broadening at higher angles, but an estimate of the LUMO+1 is 3 m_e for $T_D = 140$ K at a 2 ML thickness.

The $n = 1$ IPS effective mass for 1 and 2 ML is 1.1 m_e for $T_D = 450$ K and increases slightly to 1.3 m_e at 4 ML. The $n = 1$ effective mass is nearly a free electron mass and does not interact significantly with a crystalline layer. This is also inferred from the constant binding energies, as discussed previously. An amorphous 1 ML surface at $T_D = 140$ K increases the effective mass of the $n = 1$ IPS to 2.4 m_e due to surface roughening; similarly, the $n = 1$ effective mass for $T_D = 300$ K is 1.3 m_e (fig. 7b).

3.3 Lifetimes

A time delay between pump and probe pulses enabled the acquisition of dynamical information for each intermediate state. The decay times of each state were determined by finding the amplitude of each peak at each time delay and then fitting the peak amplitudes vs. time delay. The amplitudes of the IPS and LUMO+1 were fit to an exponential rise and decay, whereas the dynamics of the low kinetic energy scattering at low T_D could also be fit to a bi-exponential decay or a stretched exponential decay. The dynamical fits were convoluted with a Gaussian instrument function, typically on the order of 150 fs, which renders precise time constants for less than about 30 fs as physically meaningless.

The decay constants for the IPS were consistently less than the time resolution of our experiment. If an IPS electron is pushed away from the surface by increasing the layer thickness, the lifetime will increase because of the decreased overlap between the $n = 1$

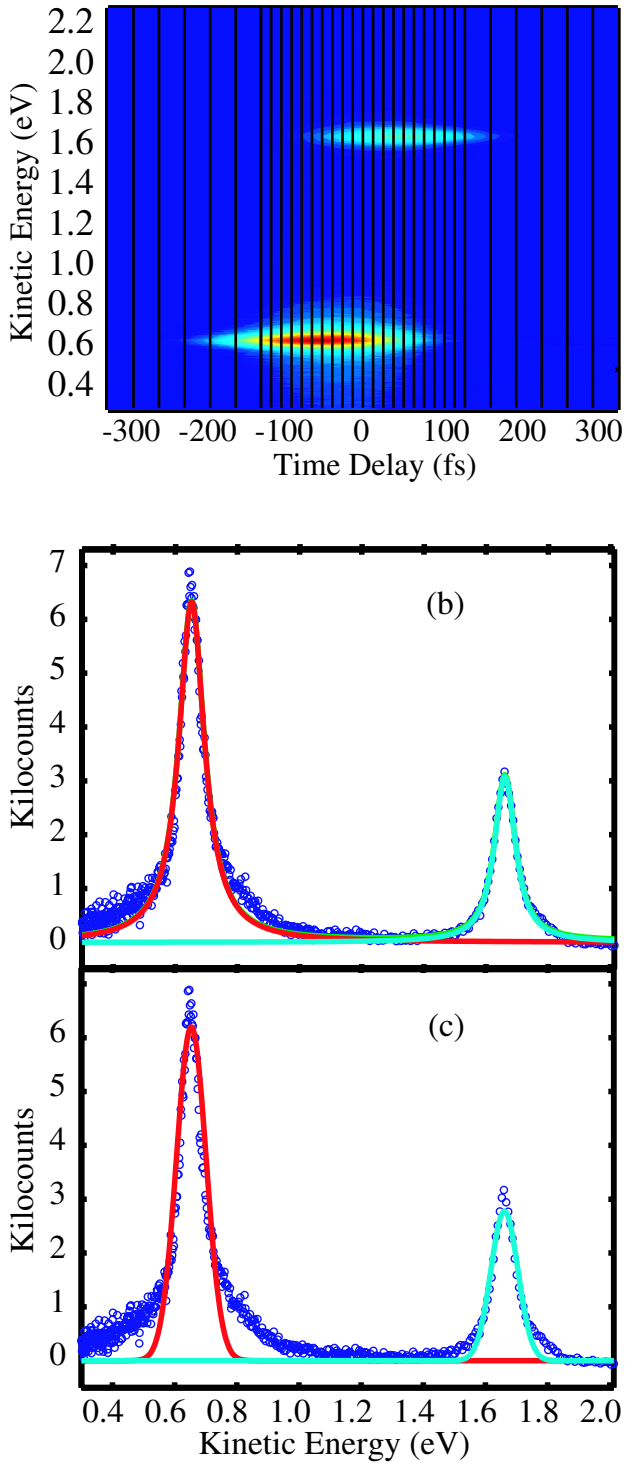

Figure 8: Each vertical line in the contour plot is a time slice corresponding to a 2PPE spectrum at a given time delay. The time delay is plotted with positive time indicating the probe pulse ($h\nu_2$) at a positive delay with respect to the pump pulse ($h\nu_1$). For 2 ML annealed at T_D = 450 K, the LUMO+1 is best fit to a Lorentzian (b) with a full width at half maximum of 90 meV, which can be converted to a lifetime or scattering time of 46 fs. The fit is better as a Lorentzian than a Gaussian lineshape (c), which suggests that the lifetime broadening is homogeneous.

T_D		2 ML	3 ML	4 ML	5 ML	6 ML	7 ML	8 ML
450 K	τ_R (fs)	31±9	35±14	50±14	41±10	40±12	34±17	38±11
	τ_D (fs)	44±10	43±14	50±14	41±10	47±10	48±10	46±10
300 K	τ_R (fs)	< 30	<30	< 30	< 30	< 30	< 30	< 30
	τ_D (fs)	72±39	73±23	110±22	131±37	131±43	143±27	140±43
200 K	τ_R (fs)	43±18	< 30	< 30	< 30			
	τ_D (fs)	63±16	89±10	135±51	194±56			
140 K	τ_R (fs)	< 30	< 30					
	τ_D (fs)	37±33	120±59					

Table 2: Rise and decay constants for the LUMO+1 in a Stranski-Krastanov morphology were dominated by interaction with the wetting layer and stayed constant, but the decay constants for amorphous layer-by-layer growth increased dramatically. For all coverages, one monolayer dynamics could not be fit reliably due to weak dynamical signal.

	4 ML	5 ML	6 ML	7 ML	8 ML
τ_{D_1} (fs)	86±64	79±32	158±65	148±49	203±41
τ_{D_2} (ps)	2.5±0.6	2.7±1.2	10±4	44±4	30±14

Table 3: The lifetimes of the low kinetic energy manifold at $T_D = 200$ K exhibit bi-exponential behavior from 4 – 8 ML.

IPS wavefunction and the silver surface. In *p*-xylene/Ag(111) layers, for example, the IPS decay constants for 1, 2, and 3 ML are 10, 40, and 1000 fs[27]. The short decay constant for the $n = 1$ IPS in coverages of crystalline PTCDA layers beyond 2 ML suggests decay predominantly influenced by interaction with the exposed 2 ML wetting layer, instead of decay through thicker PTCDA islands.

Comparing across morphologies, LUMO+1 lifetimes at thicker coverages were strongly anti-correlated with crystallinity. While crystalline systems exhibited little change in lifetimes with increasing coverage, decay constants for layers with lower T_D and rough surface morphology sharply increased (Table 2). For spectra for which the low kinetic energy manifold was present, the LUMO+1 was fit to a Lorentzian, and the manifold was fit to the tail end of a Lorentzian (fig. 9(a)). At thicker, amorphous coverages, however, separating the LUMO+1 from the low kinetic energy scattering proved intractable.

At $T_D = 200$ K, the decay constants of the low kinetic energy scattering exhibit bi-

exponential behavior beginning at 4 ML (Table 3). For $T_D = 140$ K, the low kinetic energy scattering also exhibits bi-exponential decay beginning at 4 ML with an initial decay constant of 103 fs and a secondary decay constant of 1.6 ps (fig. 9b). At 5 ML, the primary decay constant is 112±55 fs, but the secondary decay constant increases to 5.6±0.9 ps (fig. 9c). For 6, 7, and 8 ML, the decay dynamics at $T_D = 140$ K are best fit to a stretched exponential, i.e., the Williams-Watts function, of the form:

$$A = A_0 e^{-(\frac{t}{\tau_W})^\beta}, \tag{4}$$

where $0 < \beta \leq 1$ and τ_W is analogous (but not equivalent) to τ_D. A stretched exponential can be interpreted as a superposition of exponential decays, in which case a lower β suggests an increasingly broad range of decay constants [36]. For 6, 7, and 8 ML, β is 0.17, 0.16, and 0.12, respectively. In an amorphous layer with many local environments, a broad distribution to be expected, and the observed trend in β is toward a wider distribution as the layer thickness increases, although we hesitate to place greater physical significance on β.

3.4 Implications for Charge Transport Measurements

As shown above, both the band structure and dynamics of organic ultrathin films can depend critically on their morphological properties. To demonstrate the importance of this, consider the transport properties of PTCDA. Since the electronic structure of PTCDA strongly retains its intramolecular character, a nearest neighbor tight-binding approximation provides insight into its steady state transport properties. In a tight-binding model, the dispersion relation is given by:

$$E(k_\parallel) = E_0 - 2t\cos(k_\parallel a), \tag{5}$$

where t is the transfer integral and a is the lattice-spacing. Re-writing the effective mass as

$$\frac{1}{m^*} = \frac{1}{\hbar^2}\frac{\mathrm{d}^2 E}{\mathrm{d}k^2}, \tag{6}$$

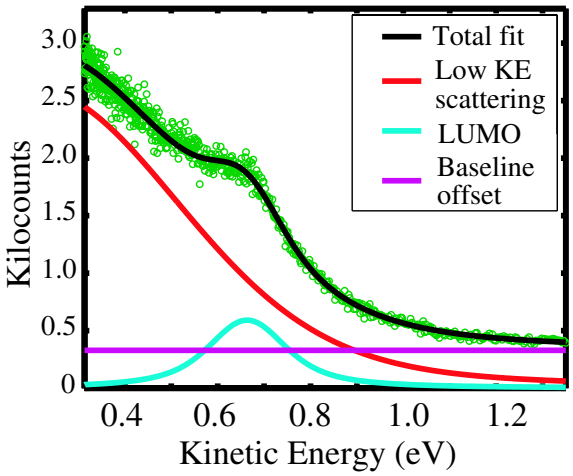

(a) Low kinetic energy manifold.

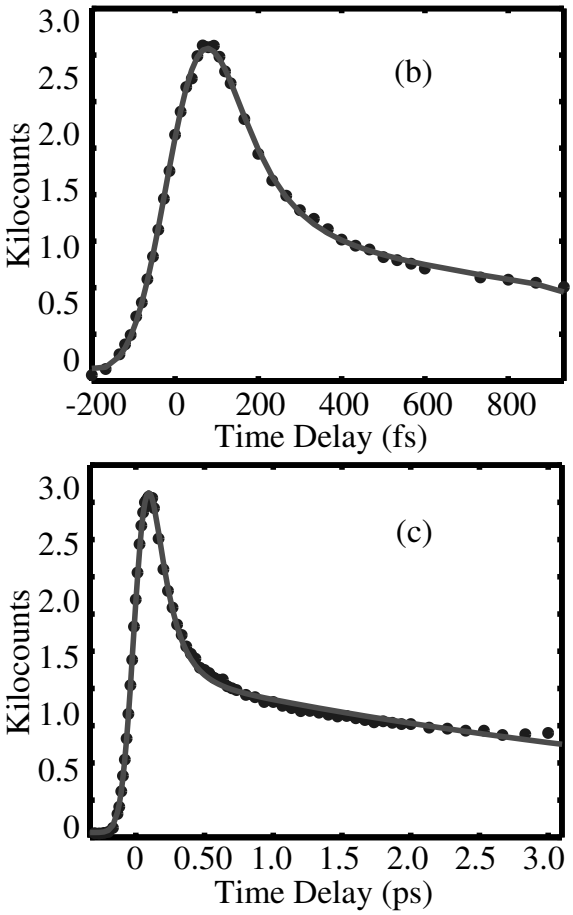

Figure 9: (a) The long-lived time dynamics of the low kinetic energy manifold could be calculated by fitting the manifold to the tail end of a Lorentzian, in addition to fitting the LUMO+1 peak to a Lorentzian. (b) For 4 ML at $T_D = 140$ K, the manifold exhibited bi-exponential decay dynamics, with $\tau_1 = 103$ fs and $\tau_2 = 1.6$ ps. (c) For 5 ML, the manifold decay increased to $\tau_1 = 1212 \pm 55$ fs and $\tau_2 = 5.6 \pm 0.9$ ps.

in the limit of small $k_{\|}$ it can be shown that[38]:

$$t = \frac{\hbar^2}{2a^2 m^*}. \tag{7}$$

This assumes that the surface band structure can be modelled with a cosine band and has a minimum at the $\overline{\Gamma}$ point, which is true for the rectangular lattice of PTCDA on Ag(111)[15]. Equation 5 has been used successfully in previous organic electronics systems including pentacene[37] and bis(1,2,5-thiadiazolo)-p-quinobis(1,3-dithiole) (BTQBT)[38], as well as $k_{\perp}$ for PTCDA layers on MoS_2[39]. As a measure of orbital overlap in crystalline layers, the transfer integral t from Eq.(7) is 25 meV using an effective mass of 0.52 m_e and 14 meV using an effective mass of 0.96 m_e. We use an averaged lattice constant of 17 Å since our experiment measures several orientations of the rectangular lattice.

Measurements of decay time and effective mass also affect estimates of charge mobility μ, where

$$\mu = \frac{e\tau}{m^*}. \tag{8}$$

The time constant τ reflects the momentum relaxation time of charge carriers through scattering processes including phonon, surface, and defect interactions, as well as non-radiative decay back into the metal. Intraband relaxation has been observed for image potential states in a variety of systems via 2PPE[27, 41], but in PTCDA, electrons decay into the metal too quickly to measure intraband relaxation (fig. 10). To estimate τ, the LUMO+1 at 2 ML was fit to a Lorentzian (fig. 8) which resulted in a FWHM of 90 meV, corresponding to a time constant of 46 fs. In combination with equation 8 and an effective mass of 0.52 m_e, a mobility value of 160 $\frac{cm^2}{sV}$ is obtained at the interface. Generally, a linewidth is additive of all the scattering processes in a system, and so this mobility should be considered a lower bound. Ostrick et al.[20] measured electronic transport using a FET geometry along the planar direction of thin films of PTCDA, with values of carrier mobilities in the range from 10^{-5} – 10^{-4} $\frac{cm^2}{sV}$. The FET experiments were composed of PTCDA layers with thicknesses of 150 nm, which is roughly 50 monolayers, and the layers were measured and therefore

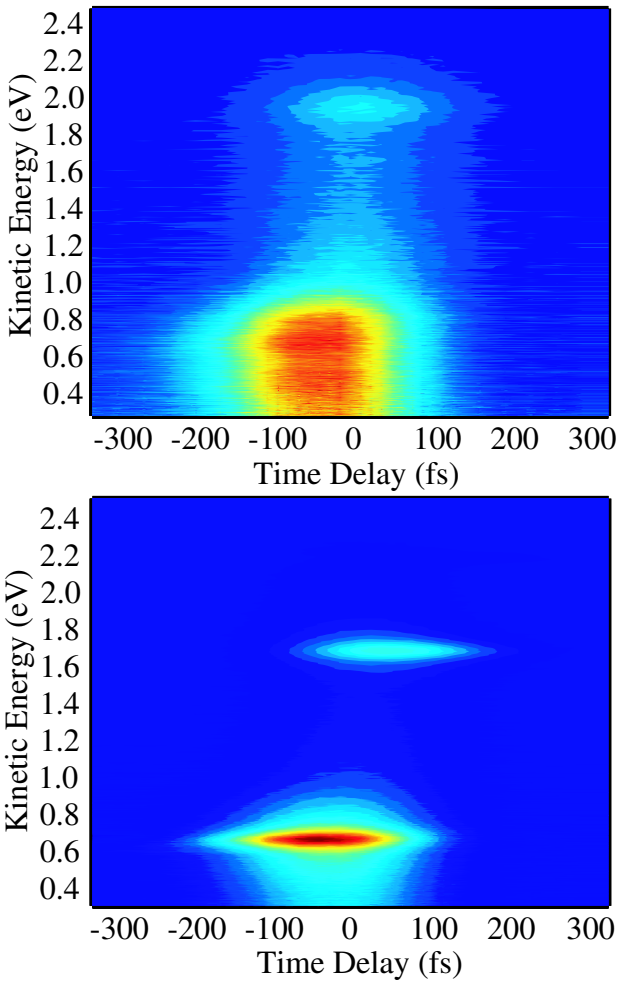

Figure 10: The contour plots compare the time dynamics of 3 ML of PTCDA with $T_D = 450$ K. The bottom figure was obtained at 0°, and the top was obtained at 24°. The similarity in dynamics for both the LUMO+1 and the higher energy $n = 1$ IPS indicate that intraband relaxation is not observable at this time scale.

annealed at temperatures up to 340 K. At this coverage, the charge transport is expected to be that of a bulk molecular crystal, and the carriers are strongly coupled to the lattice, e.g., polaronic hopping transport, which contrasts sharply with the free charge carrier we observe in interfacial layers.

In accordance with a localized carrier picture, Ostrick et al. observed temperature-dependent mobilities. Hopping mechanisms are generally attributed to polarons, but we see no evidence for lattice polaron formation in ultrathin layers of PTCDA. Ge at al. measured the formation within a few hundred femtoseconds of localized polarons in alkane layers on Ag(111)[25]. Additionally, Miller observes a shift in energy as the polar layer solvates and localizes an excited electron[40], as do Gahl et al. for H_2O and D_2O layers[42]. No solvation or dynamic localization is observed in PTCDA from 0 fs – 4 ps, nor a shift in effective mass over time (fig. 10) or over a range of temperatures from 140 K – 450 K. Therefore a transport mechanism based on lattice or molecular polarons is precluded at this interface in favor of free charge carrier transport. Free charge carriers decrease mobility at higher temperatures due to higher rates of phonon scattering; an attempt to fit a 2 ML, $T_D = 450$ K spectrum taken at 320 K to a Lorentzian lineshape resulted in a FWHM of 290 meV, which corresponds to a 14 fs relaxation time and a mobility of 24 $\frac{cm^2}{sV}$ (fig. 11). No solvation or dynamic localization exist for the image potential states as well.

4 Conclusion

Angle-resolved 2PPE spectra were collected of different morphologies and thicknesses of PTCDA on Ag(111). The morphology of the layer was found to affect the workfunction of each thin film interface and subsequent convergence to bulk PTCDA values, while the vacuum level was a function of thickness only. An initial increase in the vacuum level with the first monolayer was attributed to negative charge transfer into the metal, which was partly

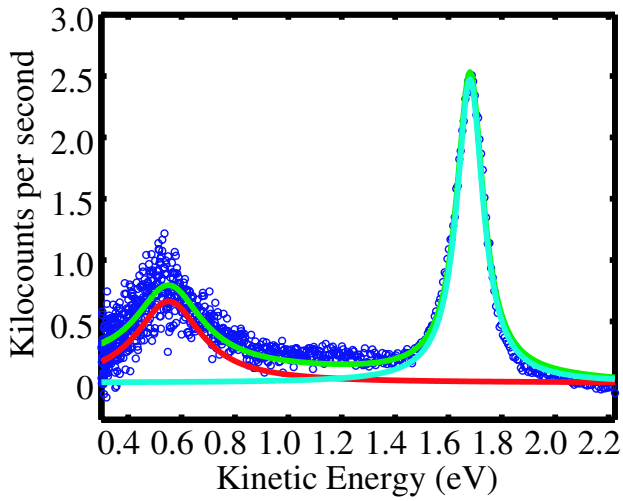

Figure 11: At 320 K, the LUMO+1 of a layer dosed at 450 K has a FWHM of 290 meV.

mitigated by the second monolayer. Effective masses were also dependent on morphology, with higher effective masses reflecting lower crystallinity. Finally, 2PPE enabled the study of electron dynamics at the PTCDA interface. Exposure to a wetting layer limited the lifetimes of electrons in crystalline layers despite high coverages of PTCDA, while amorphous layer-by-layer growth increased electron lifetimes from femtoseconds to picoseconds within a few layers. The aforementioned differences in electronic properties due to morphology emphasize the necessity of understanding interfacial structure, and attempts to build molecular devices should properly include morphological considerations in thin film engineering.

ACKNOWLEDGEMENT: This work was supported by the Director, Office of Science, Office of Basic Energy Sciences, Chemical Sciences Division of the U.S. Department of Energy, under Contract No. DE-AC02-05CH11231. The authors acknowledge NSF support for specialized equipment used in the experiments herein.

References

[1] Zhu, X.Y. *Surface Science Reports* **2004**, *56*, 1.

[2] Szymanski, P.; Garrett-Roe, S.; Harris, C. *Progress in Surface Science* **2005**, *78*, 1.

[3] Scott, J. C. *J. Vac. Sci. Technol. A* **2003**, *21*, 521.

[4] Dodabalapur, A.; Torsi, L.; Katz, H. E. *Science* **1995**, *268*, 270.

[5] Locklin, J.; Roberts, M. E.; Mannsfeld, S.; Bao, Z. *Polymer Reviews* **2006**, *46*, 79.

[6] Horowitz, G.; Hajlaoui, M. *Advanced Materials* **2000**, *12*, 1046.

[7] Knipp, D.; Street, R. A.; Völkel, A.; Ho, J. *Journal of Applied Physics* **2003**, *93*, 347.

[8] Ng, T. N.; Silveira, W. R.; Marohn, J. A. *Physical Review Letters* **2007**, *98*, 066101.

[9] Avouris, P.; Lyo, I. *Science* **1994**, *264*, 942.

[10] Li, J.; Schneider, W.-D.; Berndt, R.; Crampin, S. *Physical Review Letters* **1998**, *80*, 2893.

[11] Huang, J.; Kertesz, M. *Journal of Physical Chemistry B* **2005**, *109*, 12891.

[12] Forrest, S. *Chemical Reviews* **1997**, *97*, 1793.

[13] Tautz, F.; Eremtchenko, M.; Schaefer, J.; Sokolowski, M.; Shklover, V.; K.Glöckler,; Umbach, E. *Surface Science* **2002**, *502*, 176.

[14] Eremtchenko, M.; Schaefer, J.; Tautz, F. *Nature* **2003**, *425*, 602.

[15] Krause, B.; Dürr, A.; Ritley, K.; Schreiber, F.; Dosch, H.; Smilgies, D. *Physical Review B* **2002**, *66*, 235405.

[16] Hoffmann, M.; Schmidt, K.; Fritz, T.; Hasche, T.; Agranovich, V.; Leo, K. *Chemical Physics* **2000**, *258*, 73.

[17] Proehl, H.; Dienel, T.; Nitsche, R.; Fritz, T. *Physical Review Letters* **2004**, *93*, 097403.

[18] Goméz, U.; Leonhardt, M.; Port, H.; Wolf, H. *Chemical Physics Letters* **1997**, *268*, 1.

[19] Gebauer, W.; Langner, A.; Schneider, M.; Sokolowski, M.; Umbach, E. *Physical Review B* **2004**, *69*, 155431.

[20] Ostrick, J.; Dodabalapur, A.; Torsi, L.; Lovinger, A.; Kwock, E.; Miller, T.; Galvin, M.; Berggren, M.; Katz, H. *Journal of Applied Physics* **1997**, *81*, 6804.

[21] Tautz, F.; Eremtchenko, M.; Schaefer, J.; M.Sokolowski,; Shklover, V.; Umbach, E. *Physical Review B* **2002**, *65*, 125405.

[22] Temirov, R.; Soubatch, S.; Luican, A.; Tautz, F. S. *Nature* **2006**, *444*, 350.

[23] Ferguson, A.; Jones, T. *Journal of Physical Chemistry B* **2006**, *110*, 6891.

[24] McNeill, J.; Lingle, R.; Ge, N.; Wong, C.; Jordan, R.; Harris, C. *Physical Review Letters* **1997**, *29*, 4645.

[25] Ge, N.; Wong, C.; Jr., R. L.; McNeill, J.; Gaffney, K.; Harris, C. *Science* **1998**, *279*, 202.

[26] Petek, H.; M.J., W.; H., N.; S., O. *Science* **2000**, *288*, 1402.

[27] Garrett-Roe, S.; Shipman, S.; Szymanski, P.; Strader, M.; Yang, A.; Harris, C. *Journal of Physical Chemistry B* **2005**, *109*, 20370.

[28] Gaffney, K.; Wong, C.; Liu, S.; Miller, A.; McNeill, J.; Harris, C. *Chemical Physics* **2000**, *251*, 99.

[29] McNeill, J.; R. L. Lingle, J.; Jordan, R. E.; Padowitz, D. F.; Harris, C. B. *Journal of Chemical Physics* **1996**, *105*, 3883.

[30] Gaffney, K. J.; Miller, A.; Liu, S.; Harris, C. B. *Journal of Physical Chemistry B* **2001**, *105*, 9031.

[31] Miller, A. D.; Gaffney, K. J.; Liu, S. H.; Szymanski, P.; Garrett-Roe, S.; Wong, C. M.; Harris, C. B. *Journal of Physical Chemistry A* **2002**, *106*, 7636.

[32] Dutton, G.; Zhu, X. Y. *Journal of Physical Chemistry B* **2004**, *108*, 7788.

[33] Shipman, S.; Garrett-Roe, S.; Szymanski, P.; Yang, A.; Strader, M.; Harris, C. *Journal of Physical Chemistry B* **2006**, *110*, 10002.

[34] Hill, I.; Rajagopal, A.; Kahn, A.; Hu, Y. *Applied Physics Letters* **1998**, *73*, 662.

[35] Fauster, T.; Steinmann, W. Two-photon photoemission spectroscopy of image states. In *Photonic probes of surfaces*; Halevi, P., Ed.; Elsevier, 1995; Vol. 2. 21

[36] Lindsey, C. P.; Patterson, G. D. *Journal of Chemical Physics* **1980**, *73*, 3348.

[37] Koch, N.; Vollmer, A.; Salzmann, I.; Nickel, B.; Weiss, H.; Rabe, J. P. *Physical Review Letters* **2006**, *96*, 156803.

[38] Hasegawa, S.; Mori, T.; Imaeda, K.; Tanaka, S.; Yamashita, Y.; Inokuchi, H.; Fujimoto, H.; Seki, K.; Ueno, N. *Journal of Chemical Physics* **1994**, *100*, 6969.

[39] Yamane, H.; Kera, S.; Okudaira, K.; Yoshimura, D.; Seki, K.; Ueno, N. *Physical Review B* **2003**, *68*, 2003.

[40] Miller, A. D.; Bezel, I.; Gaffney, K. J.; Garrett-Roe, S.; Liu, S. H.; Szymanski, P.; Harris, C. B. *Science* **2002**, *297*, 1163.

[41] Chulkov, E. V.; Borisov, A. G.; Gauyacq, J. P.; Sanchez-Portal, D.; Silkin, V. M.; Zhukov, V. P.; Echenique, P. M. *Chemical Reviews* **2006**, *106*, 4160.

[42] Gahl, C.; Bovensiepen, U.; Frischkorn, C.; Wolf, M. *Physical Review Letters* **2002**, *89*, 107402.